

Synergetic Effect of Carbon Dot at Cellulose Nanofiber for Sustainable Metal-free Photocatalyst

Jungbin Ahn

Konkuk University - Seoul Campus: Konkuk University

Hyungsup Kim (✉ iconclast@konkuk.ac.kr)

Konkuk University <https://orcid.org/0000-0002-9326-9943>

Sewon pak

Konkuk University - Seoul Campus: Konkuk University

Research Article

Keywords: Carbon dot, Cellulose nanofiber, Electron transfer pathway, Photocatalyst, Fibrous structure

Posted Date: July 7th, 2021

DOI: <https://doi.org/10.21203/rs.3.rs-404493/v2>

License: © ⓘ This work is licensed under a Creative Commons Attribution 4.0 International License. [Read Full License](#)

Version of Record: A version of this preprint was published at Cellulose on October 28th, 2021. See the published version at <https://doi.org/10.1007/s10570-021-04270-2>.

Abstract

Metal-free photocatalyst was synthesized by attaching carbon dot (CD) to cellulose nanofiber (CNF) via simple *in-situ* synthesis. The graphitic core and functional groups of CD on CNF was controlled along the precursor concentration, while the fibrous structure of CNF was intact. The optical property of the samples was profoundly analyzed focusing on the electron recombination pathway. It reveals that the excited electrons in the CD transferred to the CNF and delayed the radiative recombination. The electron-hole pairs were efficiently separated in the composite where abundant amide group and sulfide bonding existed. The CD on the CNF surface improved the morphological stability of CNF under UV irradiation as well. As a result, the composite showed superior photocatalytic performance to degrade 98% of MB molecules within 25 min. The aerogel synthesized from CDCNF had good re-usability without sacrificing its photocatalytic effect. The synthesized CDCNF composite showed superior possibility for applying cellulose nanofiber to sustainable metal-free photocatalyst.

1. Introduction

Sunlight, one of the natural energy resources, is regard as promising alternative resources as it offers inexhaustible energy. Among several advances using solar energy, photocatalytic reaction is a highly encouraging technology as it could effectively degrade the environmental pollutants in air and in water. Wide range of materials were studied for photocatalyst, such as metal oxide, metal organic framework or covalent organic framework (Wang et al., 2020; He, Rong, Niu, & Cai, 2019; Zeng et al., 2020; Cheng et al., 2020). Of all materials, TiO_2 is one of the widely used photocatalyst because of its chemical inertness, high activity, low cost, and durability to chemical corrosion (Srisasiwimon, Chuangchote, Laosiripojana, & Sagawa, 2018; Lisowski et al., 2017). However, the energy absorption efficiency of bare TiO_2 is very low due to its large band gap and it needed to be supported by matrix for better recovery. To reduce the band gap, wide range of materials including metal and semiconductor were doped to crystalline TiO_2 (Guayaquil-Sosa, Serrano-Rosales, Valadés-Pelayo, & De Lasa, 2017; Gomes et al., 2011; Cai, Wu, Li, & Zheng, 2016). However, there are still critical disadvantages: most of the doping reaction needs high temperature accompanied by sintering process. Moreover, the doped metal ions can promote the electron-hole recombination and suppress the photocatalytic reactivity. Carbon-based materials such as graphite or CNT have been employed as matrix for metal oxide as well as for light absorption-assistant materials (Sharma et al., 2021; Idris et al., 2021; Ibrahim et al., 2020; Isari et al., 2020; Stan et al., 2019; Jung et al., 2018). The carbon materials can absorb light of lower energy and play the role of an electron reservoir in the system, leading to the increased efficiency of photocatalytic reaction.

Recently, numerous works have been reported to use carbon materials itself as photocatalyst. Especially carbon nitride is one of the candidates to replace metal oxide materials (Gholipour, Béland, & Do, 2017; Wang et al., 2020; Zhang, Bariotaki, Smonou, & Hollmann, 2017). It is synthesized from nitrogen-containing materials such as melamine and comprised solely of C and N bond in the form of π -conjugation. Nitrogen in the structure plays as reactive site of photocatalytic reaction. The photocatalytic performance of carbon nitride can be tuned according to the synthetic condition. For example, Oh et al. controlled the temperature for carbon nitride synthesis with direct heating method and sequential heating method (Oh et al., 2018). They revealed the sequential heating of urea could increase the grain size and reactive site for photocatalytic reaction. Another method to increase the reactive surface area is to reduce the size of carbon materials. Nano-size carbon nitride dot was also applied to photocatalytic materials. Yadav et al. synthesized carbon nitride dots (g-CNQDs) using melamine and zation at 350 °C (Yadav et al., 2019). Without metal

supporter, the synthesized g-CNQDs exhibited high performance toward reactive oxygen species (ROS) generation. However, it still needs high temperature over 300 °C to precisely control the structure of carbon nitride.

Compared to carbon nitride dot, carbon dot can be prepared with mild condition. Generally, various organic materials can be utilized as precursors and hydrothermally carbonized under 200 °C. Carbon dot has excellent optical and electrical features, acting as light absorber and electron reservoirs. Many researchers reported carbon dot as highly efficient photocatalytic materials (Duarah, & Karak, 2017; Martindale, Hutton, Caputo, & Reisner, 2015; Sarma, Majumdar, & Sarma, 2019; Li et al., 2010). However, it is hard to handle and to re-use because of its nano size. For the recovery, carbon dot was supported by matrix such as metal particles (Zeng et al., 2018; Ryu, Lee, Lee, & Jang, 2014).

In this study, metal-free photocatalyst were synthesized via green hydrothermal treatment. Nitrogen and sulfur doped carbon dot (CD) was synthesized and attached to cellulose nanofiber (CNF). The CNF played as trap for excited electron and delayed the electron-hole recombination in the system. CNF with CD on the surface was synthesized into aerogel and showed excellent photocatalytic power. It degraded ~ 98% of pollutant in 25 min without sacrificing the shape.

2. Experimental Section

2.1 Materials

Tempo-oxidized cellulose nanofiber (CNF) suspension (1.8 wt% in water, carboxylate content: $1.7 \text{ mmol}\cdot\text{g}^{-1}$) was purchased from ANPOLY (Republic of Korea). Glutathione (GT) and citric acid (CA) for the precursors of CD, Methylene blue (MB, 82% dye content), *N, N*-diethylaniline (DEA), *tert*-butanol (*t*-BA) and *para*-benzoquinone (*p*-BZQ) were purchased from Sigma Aldrich. Co (USA). CNF and GT were stored at 2 °C before use and all the other chemicals were used without any treatment.

2.2 Synthesis of carbon dots (CD)

The carbon dot in this study was prepared via hydrothermal carbonization of GT and CA. Briefly, 0.1, 0.3 and 0.5 mmol of each precursor (GT and CA) was dissolved in 30ml distilled water, together. For the synthesis, the mixture was hydrothermally carbonized at 120 °C for 4 h in a Teflon-lined autoclave. After the hydrothermal reaction, the obtained CD was purified by dialysis using a membrane (0.5-1 kDa, Biotech CD Tubing) against water for 24 h. According to the precursor amount, the synthesized carbon dot was named as 1CD, 3CD and 5CD, respectively. For example, 1CD represents the carbon dot synthesized of 0.1 mmol of GT and CA.

2.3 in-situ synthesis of CD at CNF

The CD was synthesized on the CNF's surface according to the previously reported protocol (Ahn, Pak, Song, & Kim, 2021). As same to CD synthesis procedure, 0.1, 0.3 and 0.5 mmol of each precursor was carefully dissolved in 35.5 g of CNF suspension. The mixture was poured in a Teflon-lined autoclave and reacted at 120 oC for 4 h for the in-situ synthesis of CD at CNF. The prepared suspensions were diluted to 150 ml and stirred for over 3 h, and then filtrated by a nylon filter paper (0.45 μm) for purification. The synthesized composites and the CNF were prepared in a suspension state as well as in an aerogel state via freeze-drying. The *in-situ* synthesized CD at CNF composites were named as 1CDCNF, 3CDCNF and 5CDCNF, as following the CD precursor concentrations. The

carbon dot in the composite was differently named as CD@x-CDCNF. For example, CD@1-CDCNF refers to the carbon dot in 1CDCNF composite.

2.4 Photocatalytic activity measurements

MB, a typical cationic dye was used as a model material to evaluate photocatalytic activities of the CDCNFs. For the test, 0.5 wt% of the catalyst suspensions (CNF and CDCNFs) and 5 ppm MB were mixed. Mercury lamp (1000 W) was used as the light sources and the distance between the light and the sample was set as 3 cm. Before the test, the mixtures were kept at dark for 20 min for MB absorption on catalysts. The MB concentration was measured by UV-vis absorption measurement.

2.5 Characterizations

The morphologies of the prepared samples were observed using high-resolution transmission electron microscopy (TEM) images (JEM-F200, JEOL, Japan) at 80 kV. For chemical structure analysis, Fourier-transform infrared spectroscopy (FT/IR-4000, JASCO, UK) and X-ray photoelectron spectroscopy (K-alpha, Thermo Scientific, UK) were carried out. The photoluminescence (PL) properties of the samples were studied using UV-vis absorption spectroscopy (Cary 60 UV/vis spectrophotometer, Agilent Technologies, USA) and PL spectroscopy (FS-2, SICNCO, Republic of Korea). Fluorescence lifetimes were obtained by time-correlated single photon counting method (TCSPC, Fluo Time 200 instrument, Picoquant, Germany). A 342 nm pulsed LED with a repetition rate of 5 MHz was applied for excitation. The decay profiles were analyzed by FluoFit Pro software using exponential fitting models through deconvolution with instrumental response functions (IRF).

3. Results & Discussion

CDs were synthesized by changing the precursor concentration and their structures were studied (Fig. 1). In the TEM images, CDs were individually separated and their diameters became larger as the precursor concentration increased (Fig. 1 (a)). The diameter increase was dependent on the synthesizing mechanism of carbon dot, especially nuclear growth procedure. Hydrogen bonding between the citric acid promoted the construction of the core of CD (Dong et al., 2012). The core grew by consuming the molecules in the system. The molecules in the thin solution (1 mmol of precursor) had very rare chance to contact with the other molecules. When the solution got thicker, the molecules had better chance to be grow, resulting in bigger size.

Regardless of the concentration, all the precursors were successfully reacted to each other into CDs, as seen in FT-IR result (Fig. 1 (b) & Fig. S1). All the CDs had peaks such as O-H, N-H bonding (3400 cm^{-1}), carboxyl (1714 cm^{-1}), amine (1670 cm^{-1}), amide (1108 cm^{-1}) and sulfonate/sulfide groups ($1000\text{--}1400\text{ cm}^{-1}$), as coincident to our previous work (Ahn, Pak, Song, & Kim, 2021). The functional groups of CDs had no significant difference. However, the peak for sulfonate group of 5CD was smaller than those of 1CD and 3CD (colored in orange). The decrease of sulfonate group in 5CD will be discussed further in XPS analysis (Fig. 1 (c) & S2).

Difference in the number of the molecules in unit volume led to difference in chemical structure of CD. The N1s and S2p speciations of CDs were shown in the figure. Most of the nitrogen was formed in amino N in all the CDs. Graphitic N was barely developed with 1 mmol of precursors. Nitrogen in the thin solution was hard to be conjugated into core structure since the contact between the molecules was hard. As the precursor amount increased as 3 mmol, nitrogen was combined into the graphitic structure. Nitrogen could be easily participated in core growth owing to the increased contact chance as well as the similar atomic size with carbon. The graphitic N

speciation of 5CD was slightly decreased compared to 3CD because of the competitive structure formation between nitrogen and sulfur. The big atomic size makes sulfur hard to be penetrated the core structure. Instead of penetration, sulfur was developed as sulfide bonding at the edge and sulfonate group on the surface. As the reacting solution got thicker, the content of sulfide bonding was gradually increased while sulfonate group was decreased. With more chance of contact, more sulfur was combined with carbon at the edge.

Figure 1. Characterization of CDs (a) TEM images (b) FT-IR (c) nitrogen and sulfur speciations of CDs

Based on the CD development mechanism, the structure of CDCNF composite was further studied. In Fig. 2 (a), XRD profiles were shown to study the effect of *in-situ* synthesis on the CNF physical structure. All the sampled had cellulose β crystal structure, indicating the hydrothermal treatment condition was not severe to destruct the crystalline structure of CNF. However, the crystallinity of the CDCNFs were changed. The crystallinity of the CNF was obtained as 62%, calculated by peak height method (Park et al., 2010). After the hydrothermal treatment, the crystallinity was increased. The crystallinity of CDCNFs was 75, 86 and 86% with 1, 3 and 5 mmol of CD precursors. Amorphous region can be more rapidly degraded compared to crystalline region resulted in the crystallinity increase. Citric acid in the reactor helped to break down more cellulose chain. The crystallinity did not increase over 3 mmol of citric acid. The citric acid promoted the degradation up to a certain amount, but the excessive amount did not affect the degradation significantly.

The morphologies of the CNF and the CDCNF were observed using TEM and shown in Fig. 2 (b). The CNF was highly entangled because of its high aspect ratio. The CDCNFs became less entangled after the *in-situ* synthesis treatment. The degradation of amorphous region during the hydrothermal carbonization reduced the CNF length, resulted in lower entanglements. Still the process conditions were not severe to destroy the fibrous structure. As shown in the high magnification images, CD was developed on the CNF surface (Fig. S2). The CD on the CNF was individualized with spherical shape for the all-precursor concentrations. Via the *in-situ* synthesis, CDs were successfully attached to the CNFs, regardless of the precursor concentration.

Figure 2. (a) XRD profiles and (b) TEM images of CNF and CDCNFs

The chemical structure of CDCNFs were characterized using FT-IR and XPS (Fig. 3 & Fig. S2.) The CNF had fingerprint region of cellulose as well as carboxylate group peak at 1606 cm^{-1} , which are typical in tempo-oxidized cellulose nanofiber (Fig. 3 (a)). In the process of tempo-oxidization, the glucose unit is partially changed into glucuronate group, containing carboxylate group on the C6 position. All the CDCNFs had the distinct fingerprint region of cellulose in FT-IR spectra as like to the CNF. The detailed peaks from CDs such as sulfonate groups were not clearly observed due to its small amount. However, the carboxylate group of the CNF was remarkably changed after the *in-situ* synthesis. The peak at 1606 cm^{-1} was decreased while the peak at 1719 cm^{-1} (colored in orange) was increased in all the samples. The increased peak was originated from the functional groups of CDs, such as carboxyl groups and amino groups. Glucuronate groups can be decomposed easily by mild hydrothermal carbonization because it is less stable than glucose group. During the *in-situ* synthesis, the decomposed glucuronate fragments were participated in CD-core growth and attached to the CNF surface. The peak at 1719 cm^{-1} in 1CDCNF was smaller than 3CDCNF and 5CDCNF. As discussed above, more cellulose (including glucuronate group) were degraded with higher precursor concentration. More CDs were attached to the CNF surface in 3CDCNF and 5CDCNF. The shoulder peak at 1604 cm^{-1} (colored in green) was increased as well. The peak was driven from C = O bonding of amide bond, originated from the linkage between the CD and the CNF (Ahn,

Pak, Song, & Kim, 2021). It was clear that CD was attached to the CNF by sacrificing the carboxylate group and linked by amide bonding.

XPS analysis was conducted to study the chemical structure of CD@CDCNFs (Fig. 3 (b) & Fig. S2). Interestingly, the N1s and S2p speciations of CD@CDCNFs showed similar results to CDs except for CD@1-CDCNF. In the *in-situ* synthesis, the presence of CNF certainly affected the CD structure development with 1 mmol of precursor. Graphitic N structure was more developed and sulfur was barely functionalized in the CD@1-CDCNF. Bonding formation between sulfur and the carbon core was disturbed by the CNF. Without competing to sulfur, nitrogen penetrated the core structure easily and developed graphitic N structure. With equal or more than 3 mmol of precursors, the N1s and S2p speciations of CD@CDCNF followed the tendency of CD: the graphitic N contents was highest in CD@3-CDCNF and the formation of sulfide bond predominated over sulfonate groups in CD@5-CDCNF, as coincident to CD. In turn, the number of molecules per volume majorly influenced the chemical structure of CDs and the presence of CNF minorly affected the CD formation. The chemical structures of the CD@CDCNF were considered similar to that of CDs, except for CD@1-CDCNF.

Figure 3. Chemical structure analysis of CDCNFs (a) FT-IR spectra, (b) N1s and S2p spectra from XPS (c) nitrogen and sulfur speciations of CDCNFs

Figure 4 shows the optical properties of each sample, the UV absorption curves and the PL emission spectra. In Fig. 4 (a), all the UV absorption curve did not exhibit the absorption peak related to π - π^* transition because of the low graphitization of CDs (Ahn et al., 2019). In 1CD curve, small shoulder absorption around 350 nm was observed. As the precursor concentration increased, the absorption of CDs at 350 nm became more distinct. The absorption was from n - π^* transition arose by the functional groups such as carboxylate, amine and amino groups. As shown in Fig. S3 (a), absolute nitrogen content of 1CD was much lower than the others, resulted in weak absorption. Higher n - π^* absorption of 3CD and 5CD was achieved from nitrogen both in the core and surface. More amino N in 5CD led the stronger absorption at 350 nm. Figure 4 (b) shows the UV absorption of CDCNFs. Unlike CDs, all the curves had a smooth decreasing absorption without any apparent peak. The diverse functional groups of the CD@CDCNFs split the energy level under the π * level, leading to broad absorption (Woo, Song, Ahn, & Kim, 2020). As well the long-tailed absorption was observed originated from the geometrical feature of the CNF (Ahn, Pak, Song, & Kim, 2021). The fibrous structure of CNF scattered the light. CD@1-CDCNF couldn't strongly absorb light because of their small amount and the incident light was scattered by the CNF. With the increase of precursor amount, stronger absorption curves were observed, as coincident to CDs. Incident light was absorbed by the CDs on the surface more instead of being scattered by CNF.

Figures 4 (c) ~ (e) shows the emission spectra of the CDs. All the CDs had emission maximum at 425 nm and showed weak emission dependency on the excitation wavelength. This was driven from the sulfur-containing surface state. The sulfur functionalized surface can create electron trap site with high density, weakening the excitation wavelength dependency on PL property (Dong et al., 2013). The emission wavelength of the CDs was red-shifted when the excitation wavelength shifted from 320 nm to 380 nm. As explained in the previous reports of our groups, the emission wavelength changes at different excitation wavelengths depends on the chemical structure of carbon dot. The well-graphitized carbon core of carbon dot has strong influence on the recombination of the excited electrons (Ahn et al., 2019). When carbon dot has highly developed graphitic core, the emission wavelength is firstly blue-shifted with the increasing excitation wavelength until it reaches the emission maximum, and then red-shifted as excitation wavelength increases. In this study, no blue-shift was observed with increasing

Loading [MathJax]/jax/output/CommonHTML/fonts/TeX/fontdata.js

behavior. In turn, the radiative recombination of electron at functional groups, especially the sulfur containing group, dominantly managed the PL property of CDs. The emission behavior of the CDs were affected by anchoring to CNF (Fig. 4 (f) ~ (h)). The emission spectra of the CDCNFs became slightly broader and showed stronger emission wavelength dependency on the excitation wavelength. The anchor between the CD and the CNF led to energy level splitting. Still the emission wavelength was red-shifted along the excitation wavelength, showing that the functional groups managed the emission behavior. The changes in emission pathway will be further studied in lifetime analysis.

Figure 4. Optical properties of the samples: UV spectra of (a) CDs and (b) CDCNFs, PL spectra of (c) 1CD, (d) 3CD, (e) 5CD, (f) 1CDCNF, (g) 3CDCNF and (h) 5CDCNF

The effect of anchorage to CNF on the electron pathways of CD were investigated using lifetime decay. The obtained lifetime and the quantum yield (QY) of each sample were summarized in Table. 1. The average lifetimes were 7.47, 7.75 and 7.74 ns for 1CD, 3CD and 5CD, respectively (upper row). All the decay curves of the CDs were fitted with the short lifetime component τ_1 , and the long lifetime component τ_2 . τ_1 for all the CDs had similar value to each other, as the core structure did not have significant impact on PL emission (Ahn et al., 2019). N-doped structure did not significantly affect the core state-emission pathway although the number of electrons in π system increased. τ_2 were derived from the functional group emission (Ahn et al., 2019). Comparing to 1CD, 3CD and 5CD had significantly long τ_2 . The increase of τ_2 was derived from the increase of sulfide bonding contents. As many researchers described, oxidized sulfuric functional groups such as sulfonate group has strong electron withdrawn property (Xu et al., 2015). It effectively recombines the electron-hole via light emitting pathway. The abundant sulfonate group in 1CD rapidly recombined the electrons. On the contrary in 3CD and 5CD, un-oxidized sulfide bonding held the electrons in the excited state of CD and prolonged the lifetime τ_2 .

The chemical structure managed the QYs of the CDs as well. 3CD had high QY of 42% compared to 1CD (35%) and 5CD (32%). The contents of sulfonate group and sulfide bonding served the major effect on QY changes. The sulfonate group contents gradually decreased as the precursor concentration increased while sulfide bonding was increased. The electrons in the excited state of 1CD could effectively recombined via light-emitting pathway owing to the large sulfonate group content. Despite of the decreased sulfonate group contents, 3CD exceptionally showed the highest QY value among CDs. Large number of electrons could be excited to π^* owing to the developed graphitic N structure, resulted in increased QY (Ahn et al., 2019). 5CD had the lowest QY value as it had small sulfonate group content among the CDs. Instead of fast radiative recombination, the excited electrons in the π system moved to energy level endowed by functional groups via vibrational relaxation.

In spite of the similarity in chemical structure, the electron of *in-situ* synthesized CDs had different electron recombination pathways when attached to the CNF. The average lifetimes of 1, 3 and 5CDCNF were 2.82, 2.88 and 3.50 ns, respectively. The decay curves were fitted with two components. CD and CDCNF did not have difference in τ_1 , because the CNF did not influence on the core state emission of the CD@CDCNF. It is noteworthy that τ_2 of CDCNFs had huge decrease as CNF was introduced. Regardless of the surface states (especially the sulfur speciation) differences, the τ_2 values of CDCNFs were similar to each other. The electron recombination of the CD@CDCNFs was not controlled by the functional groups. As well, the QY of CDCNFs were dramatically decreased compared to CDs: The excited electrons were mostly recombined via non-radiative pathway. It is reasonable to assume that the decrease of τ_2 was attributed to the electron transfer from the CD to the CNF. τ_2 of CDCNFs were originated from the different surface state. As studied in

the XPS, more precursors produced more sulfide bonding in the CDs, i.e., the electrons in the π system remained for longer time in the excited state and had more chance to be transferred to the CNF. CD@5-CDCNF had abundant sulfide groups resulted in more electrons transferred to the CNF. In other words, the electron-hole pairs of CD@5-CDCNF could be efficiently separated.

Table 1
The quantum yield (QY), photoluminescence lifetime (τ_{av} , τ_1 and τ_2) of the samples

1CD	τ_{ave}	(ns)	QY (%)	3CD	τ_{ave}	(ns)	QY (%)	5CD	τ_{ave}	(ns)	QY (%)	
	7.47	τ_1	5.14	35	7.75	τ_1	5.06	42	7.74	τ_1	4.93	32
		τ_2	9.31			τ_2	12.06			τ_2	11.71	
1CD CNF	τ_{ave}	(ns)	QY (%)	3CD CNF	τ_{ave}	(ns)	QY (%)	5CD CNF	τ_{ave}	(ns)	QY (%)	
	2.82	τ_1	5.69	2.58	2.88	τ_1	5.31	10.09	3.50	τ_1	5.98	8.76
		τ_2	1.14			τ_2	1.21			τ_2	1.36	

The lifetime decay results indicates that the excited electrons from CD@CDCNFs were transferred to the CNF, owing to its electron withdrawing property. To confirm this, the changes of PL intensities were studied as the strong electron donor *N,N*-diethyl aniline (DEA, 0.88 V vs. NHE) was added to the CDCNF suspension (Fig. 5). Unlike common carbon dot, the emission intensities were barely changed as the concentration of DEA was increased (LeCroy et al., 2019; Wu et al., 2018). As an electron donor, DEA injected more electrons to the ground state of CD@CDCNFs (black dotted arrow) and excited more electrons to π^* (Fig. 5 (d)). Via vibrational relaxation, the electrons were trapped to the CNF (blue dotted arrow) and non-radiatively recombined, resulted in negligible change in PL emission. Coincident to the lifetime decay results, CNF played an essential role in electron relaxation process under UV irradiation. The trap suppressed the electron radiative recombination, hence believed to enhance photocatalytic effect.

Figure 5. PL intensity of (a) 1CDCNF (b) 3CDCNF and (c) 5CDCNF with the addition of DEA in various concentration (d) energy potential diagram of CDCNF, in the presence of DEA

Figure 6 shows the catalytic performance of the samples. For the test, Methylene blue (MB) was used as the model pollutant. The MB degradation rate along time were plotted in Fig. 6 (a), in the absence (blank) and presence of the catalysts. All the CNFs had catalytic effects against MB degradation. The CNF could degrade the dye without help of CD due to the radical generation by sacrificing itself under UV irradiation, which will be further discussed in Fig. 7. With the CD attached on the CNF surface, MB was degraded more effectively by photocatalytic reaction of CD@CDCNF. Among the CDCNFs in this study, 5CDCNF showed the highest photocatalytic power. Most of the MB molecules (~ 98%) were degraded within 25 min in 5CDCNF suspension. For the clear comparison, the photocatalytic kinetics were studied (Fig. 6 (b)). The degradation performance of MB with each catalyst were plotted with the pseudo first-order degradation equation where C_0 and C are the initial concentration and the concentration of MB at time t , respectively. The apparent rate constants (k_{app}) of MB degradation were calculated as expressed in the figure. k_{5CDCNF} was almost 3 times higher than k_{CNF} , exhibiting

The photocatalytic mechanism of the CDCNFs can be explained based on the active centers of photocatalytic reaction. The photocatalytic mechanism was schematically expressed in Fig. 6 (c). Under the UV irradiation, the electrons in CD@CDCNFs were excited and electron-hole pairs were generated (Eq. (1)). The excited electrons were radiatively recombined with the holes or transferred to the energy trap induced by the CNF (Eq. (2)). The trapped electrons were retarded to be recombined, which enhanced the photocatalytic efficiency. The separated electron and hole favored to form the active radicals: the electron generated superoxide radicals ($\cdot\text{O}_2^-$) with molecule oxygen (Eq. (3)). The hole reacted with the water absorbed on the CDCNF surface to form hydroxyl radicals ($\cdot\text{OH}$, Eq. (4)). The ROS interacted with the MB molecules and degraded MB into water and carbon dioxide (Eqs. (5) and (6)).

Two types of active-species-trapping experiments were carried out to elucidate the role of the major active species in the photocatalytic process (Fig. 6 (d)). Two radical scavengers (1 mM of *tert*-butanol (*t*-BA, as $\cdot\text{OH}$ scavenger) and *para*-benzoquinone (*p*-BZQ, as $\cdot\text{O}_2^-$ scavenger)) were separately added to each suspension before the UV irradiation. Figure 6 (d) exhibits the results of photocatalytic effect in the absence (control) and presence of the radical scavengers. In CNF and 1CDCNF suspension, the effect of the scavengers was less than $\sim 5\%$ indicating the role of $\cdot\text{OH}$ and $\cdot\text{O}_2^-$ were not significant in the MB degradation. In 3CDCNF and 5CDCNF suspension, the addition of *t*-BA had minor effect on the photocatalytic power. On the other hand, the addition of *p*-BZQ in 3CDCNF and 5CDCNF suspension suppressed the degradation efficiencies to $\sim 94\%$ and $\sim 76\%$, respectively, indicating that $\cdot\text{O}_2^-$ radical made the major contributions to the photocatalytic reaction. As discussed in the lifetime analysis, 5CDCNF had the longest lifetime among the samples as more sulfide bonding existed. This indicated that more electrons remained in the excited state and could be transferred to CNF. The more electrons transferred to CNF, the more electron-hole pairs were separated, resulting in high production of $\cdot\text{O}_2^-$ radical under UV light. Thereafter, 5CDCNF effectively and rapidly degraded the MB molecules (Fig. 6 (c), Eq. (5)).

Figure 6. Photocatalytic performance of the samples (a) relative MB concentration, (b) $\ln(C_0/C)$ versus time, (c) schematic illustration of photocatalytic mechanism of CDCNF and (d) photocatalytic efficiency of the samples in the absence and presence of scavengers

For easy handling, the composites were formed into aerogel via freeze-drying process. The photocatalytic reaction of the aerogels was tested (Fig. 7 (a)). The images of MB/aerogel solution along the UV irradiation time were displayed in Fig. S4. With all the aerogels, MB degradation occurred faster than the suspensions in early 15 min. The movement of MB molecules in the suspensions were restricted as the entangled fibrous structure of CNF caused viscosity. On the other hand, MB in the solution could be dispersed without restriction and continuously absorbed to the surface of the aerogels. As well known, the negative charged carboxylate group of CNF can highly interact with positive charged MB. Even after the CD attachment on the surface of CNF, the MB absorption-ability was maintained, leading to the faster degradation (Ahn, Pak, Song, & Kim, 2021).

Though all the aerogels showed similar morphology regardless of the precursor concentration, the degradation results of the CNF and 1CDCNF aerogels after 10 min were hard to be obtained while 3CDCNF and 5CDCNF aerogels degraded most of MB within 25 min as coincident to the suspensions (Fig. S7). As shown in the images (Fig. 7 (b), S5 & S6), the morphology of CNF and 1CDCNF aerogels were severely damaged after 10 min of reaction. As mentioned, CNF could be decomposed by radicals under UV irradiation (Ma et al., 2021). During the decomposition, ROS such as hydrogen peroxide was generated as side reactant, leading to the sequential

Loading [MathJax]/jax/output/CommonHTML/fonts/TeX/fontdata.js helped to degrade MB as well in the first 10 min. However,

the further decomposition of the CNF made aerogel lost its shape. The self-decomposition of CNF was greatly suppressed in 3CDCNF and 5CDCNF aerogel, owing to the CD on the surface (Fig. S5). The UV light was absorbed by CD@CDCNF and the decomposition of the CNF was inhibited. As shown in the images, 3CDCNF and 5CDCNF aerogel retained its shape even after the reaction for 25 min. With simple wash with ethanol, the 3CDCNF and 5CDCNF aerogel was reusable while maintaining its photocatalytic performance (Fig. 7 (c)).

Figure 7. (a) Photocatalytic efficiency of the aerogels (b) digital images of the aerogels after photocatalytic reaction and (c) recycle test results of (red) 3CDCNF and (blue) 5CDCNF

4. Conclusion

In the study, CDCNF composite was synthesized for green photocatalyst. The comparison of the chemical structure of CDs synthesized with or without CNF confirmed the CNF did not have significant influence on the CD's structural formation. The increase of the precursor concentration increased the sulfide binding and amide group contents on CD. The structural differences determined the photocatalytic performance. The sulfide bonding and amide groups extended the lifetime of excited electrons and provided the transfer pathway to the CNF's potential, which resulted in the suppression of fast electron-hole recombination. The CDCNF composite synthesized with the highest precursor concentration showed the highest photocatalytic efficiency. 98% of pollutant was degraded within 25 min by CDCNF composite. When it was fabricated as aerogel, it was reusable without sacrificing the photocatalytic performance. The sustainable metal-free CDCNF composite showed the potential to be used as a high-performance photocatalytic material for sustainable development.

Declarations

Author Contributions

Jungbin Ahn: Conceptualization, Methodology, Formal analysis, Investigation, Writing - original draft, Writing - review & editing, Visualization, Funding acquisition, Project administration. **Sewon Pak:** Formal analysis, Investigation. **Hyungsup Kim:** Supervision, Writing - review & editing, Funding acquisition, Project administration

Conflicts of interest

There are no conflicts to declare.

Compliance with Ethical Standards

The work described in this article did not involve human participants and or animals.

Acknowledgements

This work was supported by National Research Foundation of Korea (NRF) funded by the Ministry of Science (Grant No. [2020R1A6A3A13075205](#) & [2020R111A2069032](#)).

References

1. Ahn J, Pak S, Song Y, Kim H (2021) In-situ synthesis of carbon dot at cellulose nanofiber for durable water

Loading [MathJax]/jax/output/CommonHTML/fonts/TeX/fontdata.js Polym 255:117387.

<https://doi.org/10.1016/j.carbpol.2020.117387>

2. Ahn J, Song Y, Kwon JE, Lee SH, Park KS, Kim S, Woo J, Kim H (2019) Food waste-driven N-doped carbon dots: Applications for Fe³⁺ sensing and cell imaging. *Mater Sci Eng C* 102:106–112. <https://doi.org/10.1016/j.msec.2019.04.019>
3. Cai J, Wu X, Li S, Zheng F (2014) Synthesis of TiO₂@ WO₃/Au nanocomposite hollow spheres with controllable size and high visible-light-driven photocatalytic activity. *ACS Sustain Chem Eng* 4(3):1581–1590. <https://doi.org/10.1021/acssuschemeng.5b01511>
4. Cheng Z, Wang L, He Y, Chen X, Wu X, Xu H, Liao Y, Zhu M (2020) Rapid metal-free synthesis of pyridyl functionalized conjugated microporous polymers for visible-light-driven water splitting. *Polym Chem* 11:3393–3397. <https://doi.org/10.1039/D0PY00249F>
5. Dong Y, Pang H, Yang HB, Guo C, Shao J, Chi Y, Li CM, Yu T (2013) Carbon-based dots co-doped with nitrogen and sulfur for high quantum yield and excitation-independent emission. *Angew Chem Int Ed* 52:7800–7804. <https://doi.org/10.1002/anie.201301114>
6. Dong Y, Shao J, Chen C, Li H, Wang R, Chi Y, Lin X, Chen G (2012) Blue luminescent graphene quantum dots and graphene oxide prepared by tuning the carbonization degree of citric acid. *Carbon* 50:4738–4743. <https://doi.org/10.1016/j.carbon.2012.06.002>
7. Duarah R, Karak N (2017) Facile and ultrafast green approach to synthesize biobased luminescent reduced carbon nanodot: an efficient photocatalyst. *ACS Sustain Chem Eng* 5(10):9454–9466. <https://doi.org/10.1021/acssuschemeng.7b02590>
8. Gholipour MR, Béland F, Do T-O (2017) Post-calcined carbon nitride nanosheets as an efficient photocatalyst for hydrogen production under visible light irradiation. *ACS Sustain Chem Eng* 5(1):213–220. <https://doi.org/10.1021/acssuschemeng.6b01282>
9. Gomes Silva C, Juárez R, Marino T, Molinari R, García H (2011) Influence of excitation wavelength (UV or visible light) on the photocatalytic activity of titania containing gold nanoparticles for the generation of hydrogen or oxygen from water. *J Am Chem Soc* 133(3):595–602. <https://doi.org/10.1021/ja1086358>
10. Guayaquil-Sosa J, Serrano-Rosales B, Valadés-Pelayo P, De Lasa H (2017) Photocatalytic hydrogen production using mesoporous TiO₂ doped with Pt. *Appl Catal B* 211:337–348. <https://doi.org/10.1016/j.apcatb.2017.04.029>
11. He S, Rong Q, Niu H, Cai Y (2019) Platform for molecular-material dual regulation: a direct Z-scheme MOF/COF heterojunction with enhanced visible-light photocatalytic activity. *Appl Catal B* 247:49–56
12. Ibrahim YO, Hezam A, Qahtan T, Al-Aswad A, Gondal M, Drmash Q (2020) Laser-assisted synthesis of Z-scheme TiO₂/rGO/g-C₃N₄ nanocomposites for highly enhanced photocatalytic hydrogen evolution. *Appl Surf Sci* 534:147578. <https://doi.org/10.1016/j.apsusc.2020.147578>
13. Idris NJ, Bakar SA, Mohamed A, Muqoyyanah M, Othman MHD, Mamat MH, Ahmad MK, Birowosuto MD, Soga T (2021) Photocatalytic performance improvement by utilizing GO_MWCNTs hybrid solution on sand/ZnO/TiO₂-based photocatalysts to degrade methylene blue dye. *Environ Sci Pollut Res* 28(6):6966–6979. <https://doi.org/10.1007/s11356-020-10904-y>
14. Isari AA, Hayati F, Kakavandi B, Rostami M, Motevassel M, Dehghanifard E (2020) N, Cu co-doped TiO₂@ functionalized SWCNT photocatalyst coupled with ultrasound and visible-light: An effective sono-photocatalysis process for pharmaceutical wastewaters treatment. *Chem Eng J* 392:123685. <https://doi.org/10.1016/j.cej.2019.123685>

15. Jung H, Cho KM, Kim KH, Yoo H-W, AlSaggaf A, Gereige I, Jung H-T (2018) Highly efficient and stable CO₂ reduction photocatalyst with a hierarchical structure of mesoporous TiO₂ on 3D graphene with few-layered MoS₂. *ACS Sustain Chem Eng* 6(5):5718–5724. <https://doi.org/10.1021/acssuschemeng.8b00002>
16. LeCroy GE, Wang P, Bunker CE, Fernando KS, Liang W, Ge L, Reibold M, Sun Y-P (2019) Hybrid carbon dots platform enabling opportunities for desired optical properties and redox characteristics by-design. *Chem Phys Lett* 724:8–12. <https://doi.org/10.1016/j.cplett.2019.03.046>
17. Li H, He X, Kang Z, Huang H, Liu Y, Liu J, Lian S, Tsang CHA, Yang X, Lee ST (2010) Water-soluble fluorescent carbon quantum dots and photocatalyst design. *Angew Chemie* 122:4532–4536
18. <https://doi.org/10.1002/anie.200906154>
19. Lisowski P, Colmenares JC, Mašek O e, Lisowski W, Lisovytskiy D, Kamińska A, Łomot D (2017) Dual functionality of TiO₂/biochar hybrid materials: photocatalytic phenol degradation in the liquid phase and selective oxidation of methanol in the gas phase. *ACS Sustain Chem Eng* 5 (7): 6274–6287. <https://doi.org/10.1021/acssuschemeng.7b01251>
20. Ma F, Zhang S, Li P, Sun B, Xu Y, Tao D, Zhao H, Cui S, Zhu R, Zhang B (2021) Investigation on the role of the free radicals and the controlled degradation of chitosan under solution plasma process based on radical scavengers. *Carbohydr Polym* 257:117567–117574. <https://doi.org/10.1016/j.carbpol.2020.117567>
21. Martindale BC, Hutton GA, Caputo CA, Reiser E (2015) Solar hydrogen production using carbon quantum dots and a molecular nickel catalyst. *J Am Chem Soc* 137:6018–6025. <https://doi.org/10.1021/jacs.5b01650>
22. Oh J, Shim Y, Lee S, Park S, Jang D, Shin Y, Ohn S, Kim J, Park S (2018) Structural insights into photocatalytic performance of carbon nitrides for degradation of organic pollutants. *J Solid State Chem* 258:559–565. <https://doi.org/10.1016/j.jssc.2017.11.026>
23. Park S, Baker JO, Himmel ME, Parilla PA, Johnson DK (2010) Cellulose crystallinity index: measurement techniques and their impact on interpreting cellulase performance. *Biotechnol Biofuels* 3:1–10. <https://doi.org/10.1186/1754-6834-3-10>
24. Ryu J, Lee E, Lee S, Jang J (2014) Fabrication of graphene quantum dot-decorated graphene sheets via chemical surface modification. *Chem Commun* 50:15616–15618. <https://doi.org/10.1039/C4CC06567K>
25. Sarma D, Majumdar B, Sarma TK (2019) Visible-light induced enhancement in the multi-catalytic activity of sulfated carbon dots for aerobic carbon–carbon bond formation. *Green Chem* 21:6717–6726. <https://doi.org/10.1039/c9gc02658d>
26. Sharma HK, Sharma SK, Vemula K, Koirala AR, Yadav HM, Singh BP (2021) CNT facilitated interfacial charge transfer of TiO₂ nanocomposite for controlling the electron-hole recombination. *Solid State Sci* 112:106492. <https://doi.org/10.1016/j.solidstatesciences.2020.106492>
27. Srisasiwimon N, Chuangchote S, Laosiripojana N, Sagawa T (2018) TiO₂/lignin-based carbon composited photocatalysts for enhanced photocatalytic conversion of lignin to high value chemicals. *ACS Sustain Chem Eng* 6(11):13968–13976. <https://doi.org/10.1021/acssuschemeng.8b02353>
28. Stan MS, Badea MA, Pircalabioru GG, Chifiriuc MC, Diamandescu L, Dumitrescu I, Trica B, Lambert C, Dinischiotu A (2019) Designing cotton fibers impregnated with photocatalytic graphene oxide/Fe, N-doped TiO₂ particles as prospective industrial self-cleaning and biocompatible textiles. *Mater Sci Eng C* 94:318–332. <https://doi.org/10.1016/j.msec.2018.09.046>
29. Wang J, Xue L, Hong M, Ni B, Niu T (2020) Heterogeneous visible-light-induced Meerwein hydration reaction

Loading [MathJax]/jax/output/CommonHTML/fonts/TeX/fontdata.js e photocatalyst. *Green Chem* 22(2):411–416.

<https://doi.org/10.1039/C9GC03679B>

30. Wang G-B, Li S, Yan C-X, Zhu F-C, Lin Q-Q, Xie K-H, Geng Y, Dong Y-B (2020) Covalent organic frameworks: emerging high-performance platforms for efficient photocatalytic applications. *J Mater Chem A* 8:6957–6983. <http://doi.org/10.1039/D0TA00556H>
31. Woo J, Song Y, Ahn J, Kim H (2020) Green one-pot preparation of carbon dots (CD)-embedded cellulose transparent film for Fe³⁺ indicator using ionic liquid. *Cellulose* 27:4609–4621. <https://doi.org/10.1007/s10570-020-03099-5>
32. Wu W, Zhang Q, Wang R, Zhao Y, Li Z, Ning H, Zhao Q, Wiederrecht GP, Qiu J, Wu M (2018) Synergies between unsaturated Zn/Cu doping sites in carbon dots provide new pathways for photocatalytic oxidation. *ACS Catal* 8:747–753. <https://doi.org/10.1021/acscatal.7b03423>
33. Xu Q, Liu Y, Gao C, Wei J, Zhou H, Chen Y, Dong C, Sreepasad TS, Li N, Xia Z (2015) Synthesis, mechanistic investigation, and application of photoluminescent sulfur and nitrogen co-doped carbon dots. *J Mater Chem C* 3:9885–9893. <https://doi.org/10.1039/C5TC01912E>
34. Yadav P, Nishanthi S, Purohit B, Shanavas A, Kailasam K (2019) Metal-free visible light photocatalytic carbon nitride quantum dots as efficient antibacterial agents: an insight study. *Carbon* 152:587–597. <https://doi.org/10.1016/j.carbon.2019.06.045>
35. Zeng Q-R, Cheng Z-H, Yang C, He Y, Meng N, Faul CF, J, Liao Q-Z (2021) Metal-free synthesis of pyridyl conjugated microporous polymers for photocatalytic hydrogen evolution. *Chinese J Polym Sci* 39:1–9. <https://doi.org/10.1007/s10118-021-2574-3>
36. Zeng Z, Xiao F-X, Phan H, Chen S, Yu Z, Wang R, Nguyen T-Q, Tan TTY (2018) Unraveling the cooperative synergy of zero-dimensional graphene quantum dots and metal nanocrystals enabled by layer-by-layer assembly. *J Mater Chem A* 6:1700–1713. <https://doi.org/10.1039/C7TA09119B>
37. Zhang W, Bariotaki A, Smonou I, Hollmann F (2017) Visible-light-driven photooxidation of alcohols using surface-doped graphitic carbon nitride. *Green Chem* 19(9):2096–2100. <https://doi.org/10.1039/C7GC00539C>

Figures

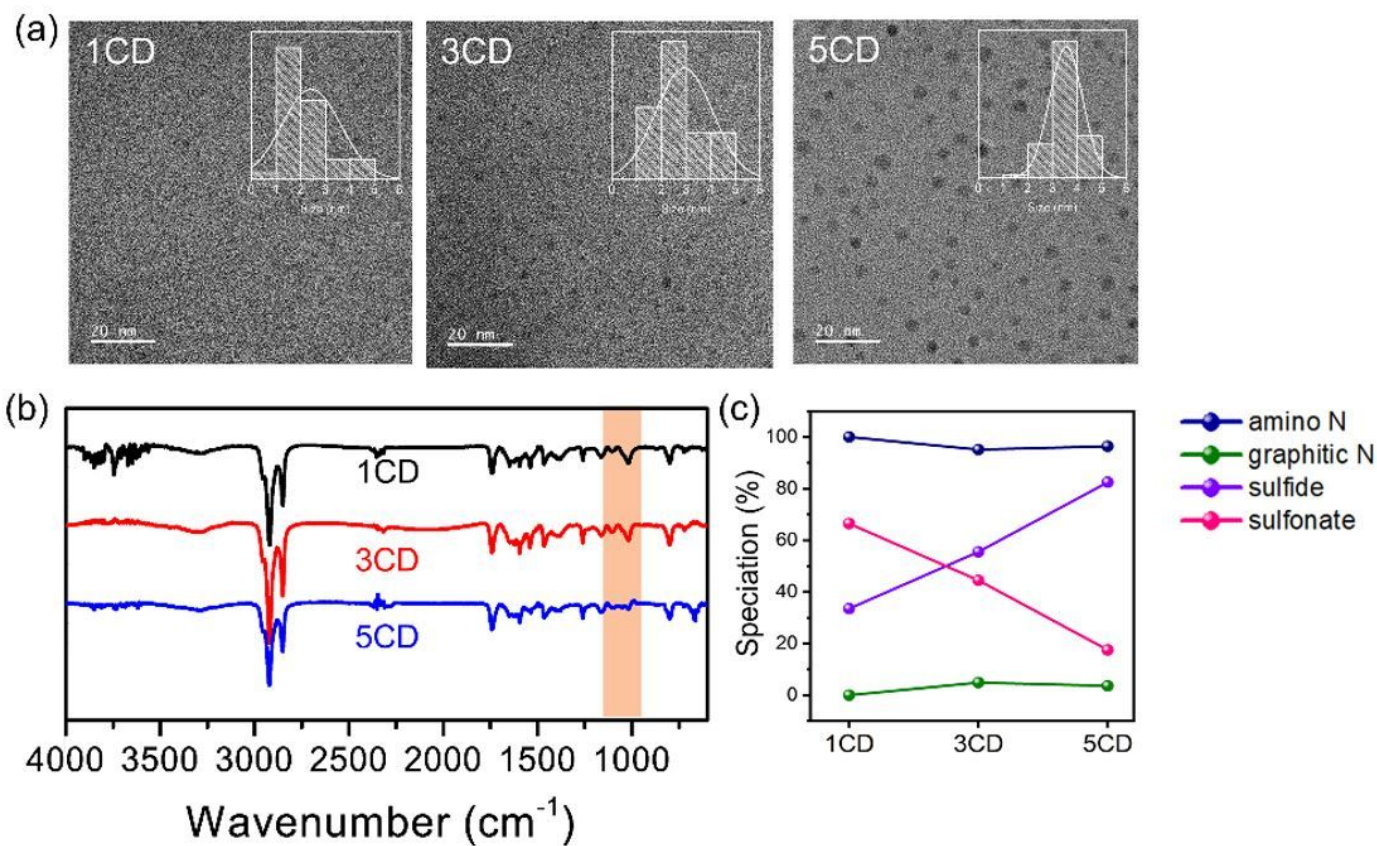


Figure 1

Characterization of CDs (a) TEM images (b) FT-IR (c) nitrogen and sulfur speciations of CDs

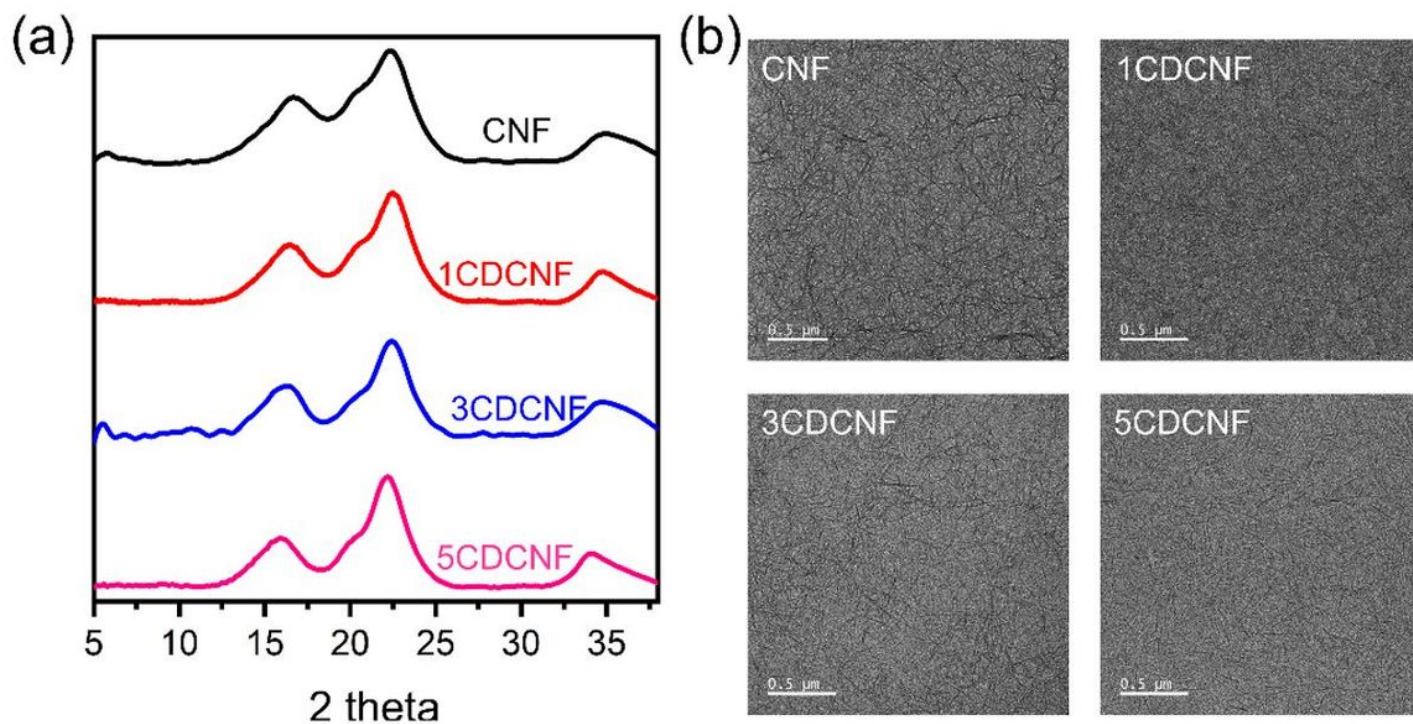


Figure 2

Loading [MathJax]/jax/output/CommonHTML/fonts/TeX/fontdata.js

(a) XRD profiles and (b) TEM images of CNF and CDCNFs

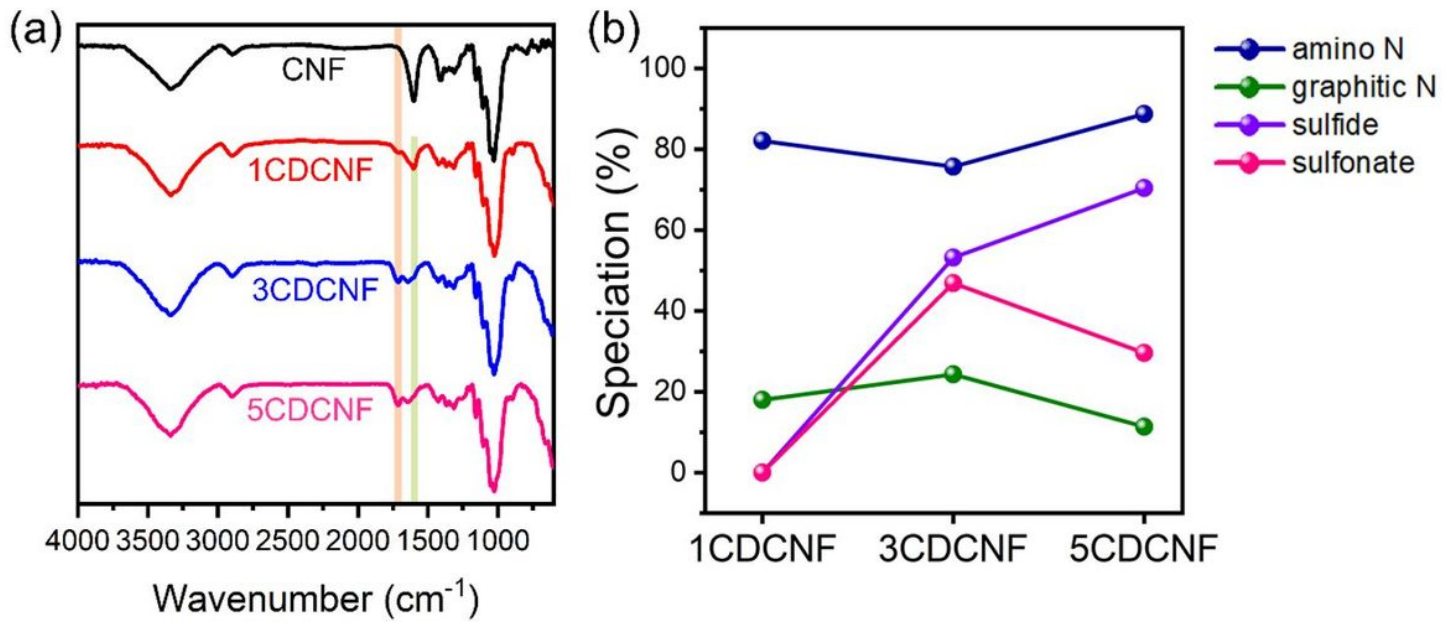


Figure 3

Chemical structure analysis of CDCNFs (a) FT-IR spectra, (b) N1s and S2p spectra from XPS (c) nitrogen and sulfur speciations of CDCNFs

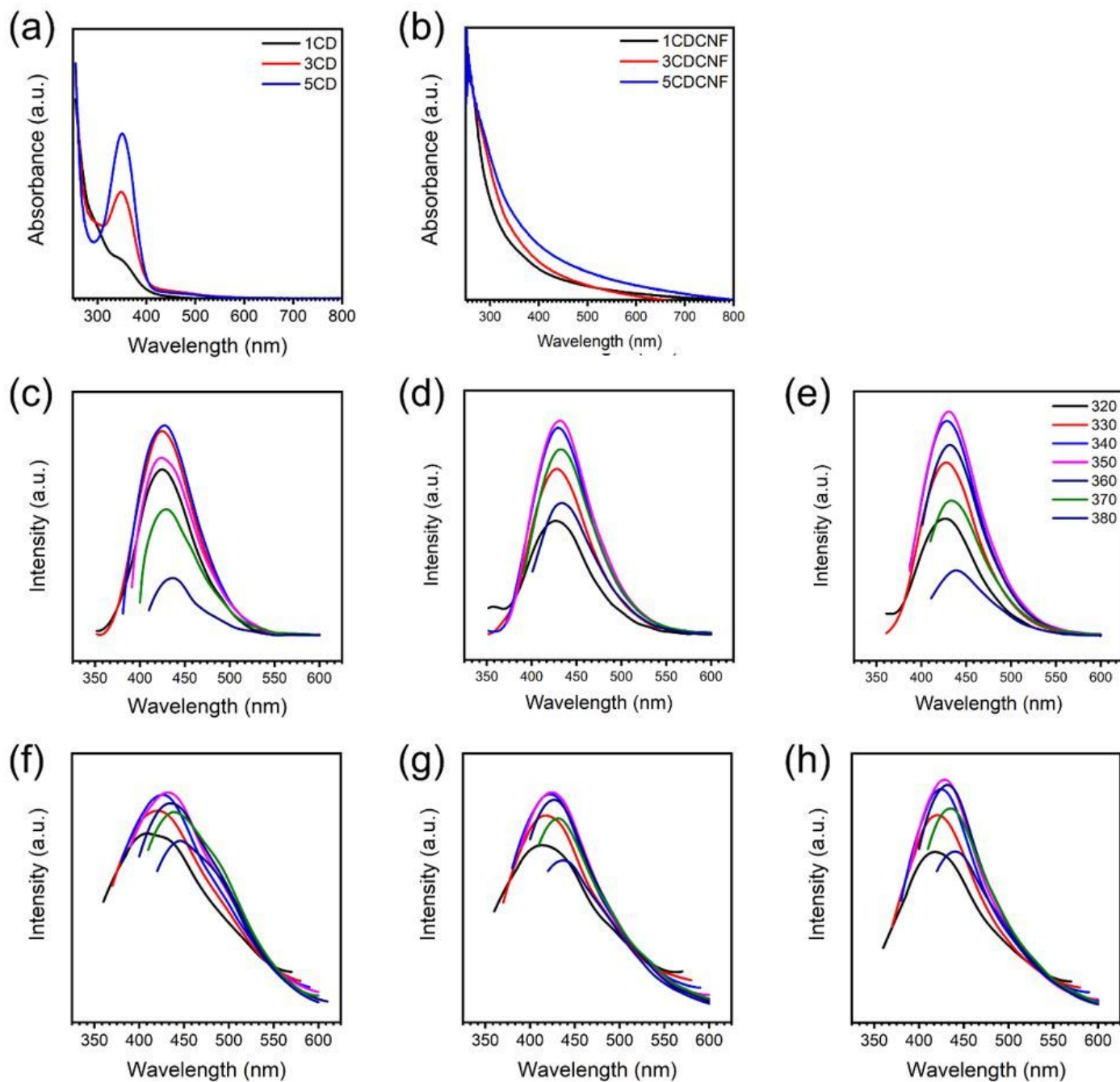


Figure 4

Optical properties of the samples: UV spectra of (a) CDs and (b) CDCNFs, PL spectra of (c) 1CD, (d) 3CD, (e) 5CD, (f) 1CDCNF, (g) 3CDCNF and (h) 5CDCNF

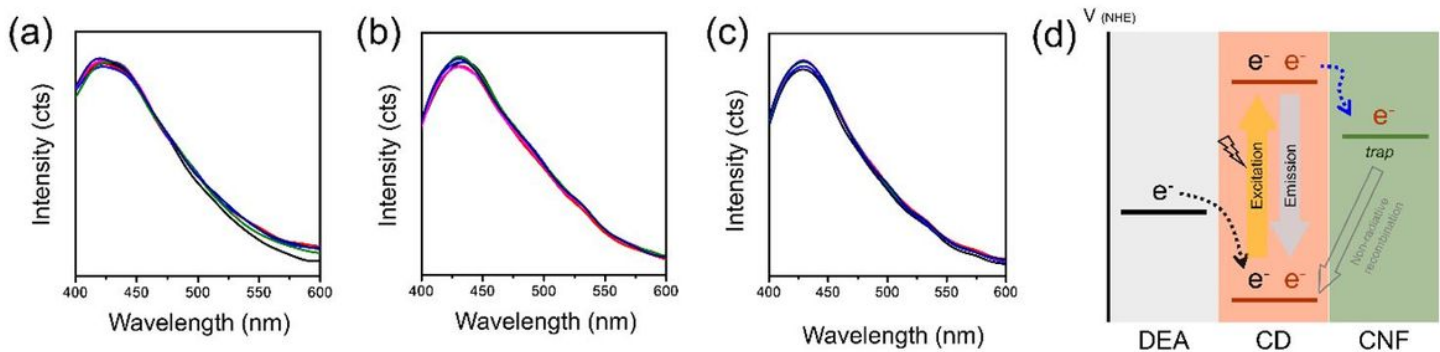


Figure 5

PL intensity of (a) 1CDCNF (b) 3CDCNF and (c) 5CDCNF with the addition of DEA in various concentration (d) energy potential diagram of CDCNF, in the presence of DEA

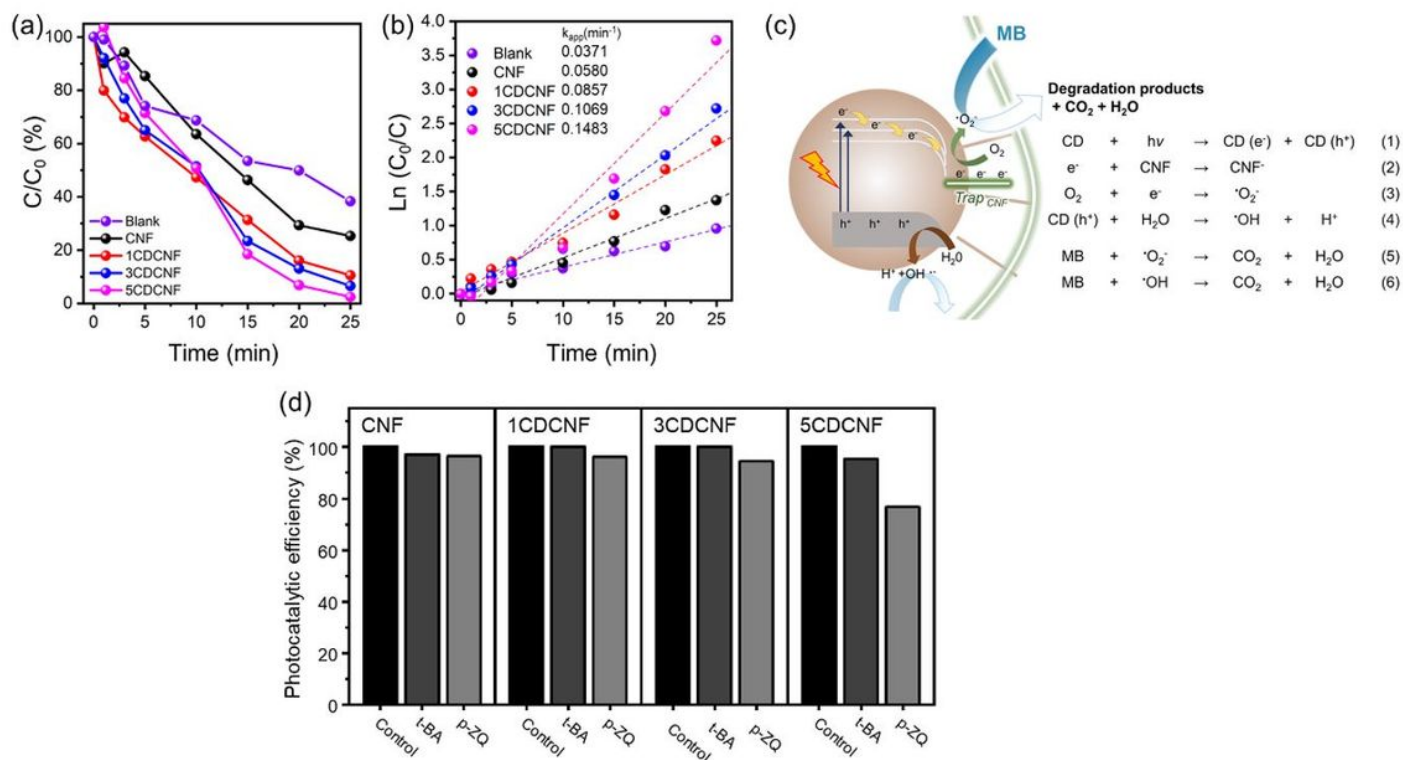


Figure 6

Photocatalytic performance of the samples (a) relative MB concentration, (b) $\ln(C_0/C)$ versus time, (c) schematic illustration of photocatalytic mechanism of CDCNF and (d) photocatalytic efficiency of the samples in the absence and presence of scavengers

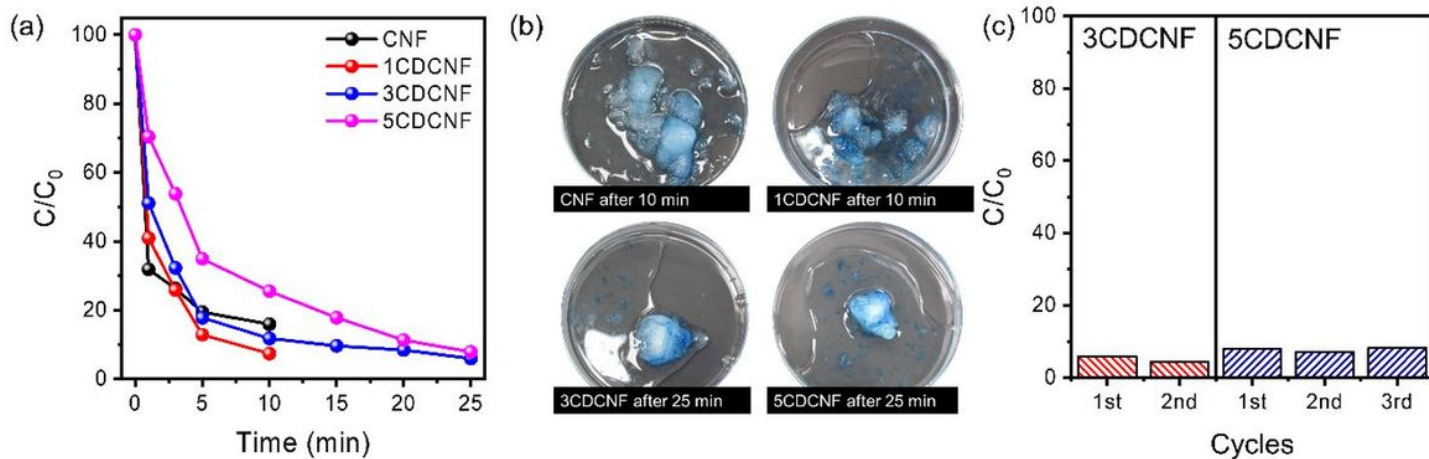


Figure 7

(a) Photocatalytic efficiency of the aerogels (b) digital images of the aerogels after photocatalytic reaction and (c) recycle test results of (red) 3CDCNF and (blue) 5CDCNF

Supplementary Files

This is a list of supplementary files associated with this preprint. Click to download.

- [graphicsabstract.jpg](#)
- [Supportingmaterials.docx](#)